

Deep Neural Networks for Modeling Astrophysical Nuclear reacting flows

XIAOYU ZHANG ^{1,2} YUXIAO YI ^{3,2} LILE WANG ^{4,5} ZHI-QIN JOHN XU ^{3,2} TIANHAN ZHANG ⁶ AND
YAO ZHOU ^{1,2}

¹*School of Physics and Astronomy, Shanghai Jiao Tong University, Shanghai 200240, China*

²*Institute of Natural Sciences and MOE-LSC, Shanghai Jiao Tong University, Shanghai 200240, China*

³*School of Mathematical Sciences, Shanghai Jiao Tong University, Shanghai 200240, China*

⁴*The Kavli Institute for Astronomy and Astrophysics, Peking University, Beijing 100871, China*

⁵*Department of Astronomy, School of Physics, Peking University, Beijing 100871, China*

⁶*School of Astronautics, Beihang University, Beijing 100191, China*

ABSTRACT

In astrophysical simulations, nuclear reacting flows pose computational challenges due to the stiffness of reaction networks. We introduce neural network-based surrogate models using the DeePODE framework to enhance simulation efficiency while maintaining accuracy and robustness. Our method replaces conventional stiff ODE solvers with deep learning models trained through evolutionary Monte Carlo sampling from zero-dimensional simulation data, ensuring generalization across varied thermonuclear and hydrodynamic conditions. Tested on 3-species and 13-species reaction networks, the models achieve $\lesssim 1\%$ accuracy relative to semi-implicit numerical solutions and deliver a $\sim 2.6\times$ speedup on CPUs. A temperature-thresholded deployment strategy ensures stability in extreme conditions, sustaining neural network utilization above 75% in multi-dimensional simulations. These data-driven surrogates effectively mitigate stiffness constraints, offering a scalable approach for high-fidelity modeling of astrophysical nuclear reacting flows.

Keywords: Neural networks (1933) — Reaction models (2231) — Nuclear astrophysics (1129) — Hydrodynamical simulations (767) — Computational methods (1965)

1. INTRODUCTION

Nuclear reacting hydrodynamic flows play a crucial role in astrophysical phenomena such as stellar evolution, supernova explosions, and extreme processes near compact objects. Numerical simulations of these flows require coupling fluid dynamics with nuclear reaction networks, including the advection of nuclear species and energy feedback mechanisms. Recent advancements in computational power and multi-physics algorithms have enabled increasingly sophisticated modeling of these systems. Current research focuses on integrating multi-scale physics to resolve challenges such as turbulent combustion, neutrino-matter interactions, and high-density equation-of-state dependencies. Numerical systems for nuclear reacting flows have been instrumental in studying double detonation scenarios [36; 16; 29; 15], deflagration-to-detonation transitions

[12; 13], white dwarf collisions [26; 14], and X-ray bursts on neutron stars [50; 21; 17].

The numerical treatment of nuclear reacting flows remains challenging due to extreme stiffness arising from the timescale separations spanning orders of magnitude between nuclear reactions. To ensure stability and accuracy, implicit or semi-implicit ordinary differential equation (ODE) solvers with adaptive step-size control are typically employed. These methods necessitate computationally expensive evaluations of reaction rate vectors, Jacobian matrices, and matrix inversions. Established simulation tools such as Castro [51], MAESTROeX [9], and FLASH [11] have adopted this paradigm, enabling critical insights into astrophysical systems over decades of development. However, prohibitive computational costs continue to limit explorations requiring finer reaction-network details or higher spatiotemporal resolutions, underscoring the need for optimized algorithms and high-performance computing strategies.

Recent advances in deep learning (DL) techniques have demonstrated potential to enhance nuclear reacting

flow simulations by replacing traditional semi-implicit solvers with data-driven surrogate models based on deep neural networks (DNNs). This approach has gained traction in combustion chemistry simulations [20], where Zhang et al. [46]; Wang et al. [41] pioneered DNN-based surrogate models capable of advancing hydrodynamic and thermochemical time steps while circumventing stiffness inherent to chemical kinetic networks. These models have been validated across diverse reacting flow scenarios, achieving order-of-magnitude speedups compared to conventional solvers without compromising accuracy. Building on this, Yao et al. [45] introduced DeePODE, a novel framework combining evolutionary Monte Carlo sampling with neural networks to tackle multi-timescale systems such as electrochemical battery thermal runaway and turbulent jet flame. Given the mathematical equivalence between nuclear reaction networks and chemical kinetics, this paradigm holds significant promise for accelerating simulations in nuclear astrophysics.

Despite these developments, the application of DL-based surrogate models to nuclear astrophysical systems remains underexplored. Fan et al. [10] demonstrated a proof-of-concept by training a DNN to replace nuclear reaction solvers in flame simulations at $\sim 10^{-1}$ cm scales involving 3 nuclear species. Although their work highlighted feasibility and computational gains, significant challenges persist in adopting such methods to high-dimensional reaction networks and extreme parameter regimes typical of astrophysical environments. In this work, we adapt the DeePODE framework [45] to address these challenges, structuring our methodology into three components: (1) Monte Carlo sampling of nuclear reaction data, (2) DNN training, and (3) validation within reacting flow simulations. Unlike prior studies, our sampling strategy is decoupled from specific flame configurations, enabling a single trained model to generalize across broad regions of parameter space without fine-tuning—a critical requirement for astrophysical applications.

This paper is structured as follows. The equations to be solved are described in §2. The neural network architecture, sampling methodology, and training procedures are presented in §3. Building on this methodological foundation, §4 conducts systematic comparisons of the calibration accuracy in the zero-, one-, and two-dimensional simulation frameworks and performs acceleration performance. Finally, §5 concludes with a summary of key findings and outlines potential directions for future research.

2. GOVERNING EQUATIONS OF NUCLEAR REACTING FLOWS

Reacting flow simulations are carried out based on hydrodynamic calculations carrying reacting species,

$$\frac{\partial(\rho X_k)}{\partial t} + \nabla \cdot (\rho X_k \mathbf{v}) = \rho \dot{\omega}_k, \quad (1)$$

$$\frac{\partial(\rho \mathbf{v})}{\partial t} + \nabla \cdot (\rho \mathbf{v} \mathbf{v} + p \mathbf{I}) = 0, \quad (2)$$

$$\frac{\partial(\rho \epsilon)}{\partial t} + \nabla \cdot [\mathbf{v}(\rho \epsilon + p)] = \rho \dot{S}. \quad (3)$$

Here ρ , p , \mathbf{v} are the mass density, the gas pressure, and the velocity, respectively, X_k is the mass fraction of species k ($\sum_k X_k = 1$), whose associated production rate is $\dot{\omega}_k$, and \mathbf{I} is the identity tensor. In Eq.(3), ϵ denotes the total specific energy and \dot{S} is the rate of generation of nuclear energy per unit mass. In this paper, these equations are solved using the Kratos framework (see Wang 39, and also §4), on which the nuclear reaction calculations are carried out.

Nuclear reactions and hydrodynamics can be coupled via the operator splitting scheme (such as Strang splitting [31]), by which they can be computed separately. The governing ODEs for nuclear reactions are:

$$\frac{d\mathbf{X}}{dt} = \dot{\omega}(T, \rho, \mathbf{X}), \quad (4)$$

$$\frac{d(\rho \epsilon)}{dt} = \rho \dot{S}, \quad (5)$$

where \mathbf{X} denotes the vector of mass fractions of species, and the production rates $\dot{\omega}$ are generally associated with the temperature T and density ρ . The temperature is updated using the equation of state (EOS). For the gamma-law EOS,

$$p = \rho \epsilon_{int} (\gamma - 1), \quad (6)$$

we adopt the ideal gas law with an adiabatic coefficient of $\gamma = 5/3$, and specific internal energy ϵ_{int} can be calculated by subtracting the specific kinetic energy from the total specific energy ϵ .

In standard computational workflows, the integral time step for advancing nuclear reaction networks is significantly smaller than that for hydrodynamic processes (namely $\Delta t_{\text{react}} \ll \Delta t_{\text{flow}}$), leading to substantial computational overhead. Therefore, this study focuses on developing surrogate models to circumvent stiffness constraints, thereby seamlessly replacing the time-consuming direct integration (DI).

In our work, we select two distinct nuclear reaction networks. The small-size network, termed Net-3Sp, is a simplified test network that includes 3 isotopes (^4He , ^{12}C , ^{16}O) and 4 reactions, as illustrated in Figure

1(a). The moderate-size network, Net-13Sp, is a more comprehensive model designed for simulations of white dwarf combustion [29]. It encompasses thirteen isotopes (^4He , ^{12}C , ^{16}O , ^{20}Ne , ^{24}Mg , ^{28}Si , ^{32}S , ^{36}Ar , ^{40}Ca , ^{44}Ti , ^{48}Cr , ^{52}Fe , ^{56}Ni) and incorporates thirty-two nuclear reactions, as depicted in Figure 1(b). This detailed network is particularly suited for modeling the complex nucleosynthesis and energy generation processes in astrophysical scenarios. The coefficients for these reaction networks are generated using the `pynucastro` [30; 43; 35], which constructs reaction networks and provides essential nuclear reaction parameters such as reaction rates.

3. DEEP NEURAL NETWORKS

3.1. Architecture

The temporal evolution of nuclear reaction under a desired time step Δt can be written as:

$$\mathbf{X}(t + \Delta t) := \mathcal{F}(T, \rho, \mathbf{X}(t)) = \mathbf{X}(t) + \int_t^{t+\Delta t} \dot{\omega} dt, \quad (7)$$

where \mathcal{F} is a non-linear propagation operator. We propose a deep neural network (DNN) model \mathcal{F}_θ to learn the mapping \mathcal{F} , and the θ denotes learnable parameters. In our work, the time step Δt is fixed. Therefore, the DNN model takes $[T, \rho, \mathbf{X}]$ as input and then predicts mass fraction species. Then, the temperature is computed through energy conservation derived from the heat release of updated species.

For the neural network structure, the feed-forward network (FFN) structure is considered in this study. Note that we employ an individual FFN for each nuclear reaction network. Each FFN comprises three hidden layers with 1,600, 800, and 400 neurons, respectively. The activation functions of hidden layers are Gaussian Error Linear Unit (GELU).

As mentioned above, the input state vector is composed of temperature, density and mass fraction of species, denoted as $\mathbf{x}(t) = [T(t), \rho(t), \mathbf{X}(t)]$ with input size being $N_s + 2$ where N_s is the species size of reaction network. The label/target state of the DNN is $\mathbf{u}(t) = [\mathbf{X}(t + \Delta t) - \mathbf{X}(t)]$ with size = N_s , representing the change of mass fraction after a constant time step Δt . The training dataset is in the form of $\mathcal{D}_{\text{train}} = \{\mathbf{x}_i, \mathbf{u}_i\}_{i=1}^N$.

During the nuclear reaction processes, the mass fractions of species exhibit typical multi-scale features. Across distinct species or different evolutionary time, the characteristic scales span multiple orders of magnitude, ranging from $\mathcal{O}(10^{-25})$ to $\mathcal{O}(10^{-1})$. Therefore, to ensure the stability of DNN training, appropriate pre-processing of raw data is required to transform the

mass fraction to near $\mathcal{O}(1)$ before directly feeding the dataset into DNNs. Logarithm transformation seems natural, but fails to handle the scenarios when the concentrations approach 0. Although we can add an offset ε to the function to avoid discontinuities at zero, another defect arises: sensitivity to perturbations. For instance, assuming $\varepsilon = 10^{-25}$ and we define the function $f(x) = \log_{10}(x + \varepsilon)$. If the input $x = 10^{-20}$ is slightly perturbed to $\tilde{x} = 10^{-30}$, this operation results in a change $\Delta f \approx 5$. Such machine-precision perturbation leads to significant fluctuation, indicating that the logarithmic transformation is ill-suited in our work.

To solve the prospective issue of multiple magnitude scales in predicting the reaction network, the Box-Cox transformation (BCT) is introduced. It is a statistical method originally proposed by Box & Cox [5] to stabilize variance of data, and the function is defined as

$$B(x) = \begin{cases} \frac{x^\lambda - 1}{\lambda} & \text{if } \lambda \neq 0, \\ \ln(x) & \text{if } \lambda = 0, \end{cases} \quad (8)$$

where x is the input variable and λ is a hyper-parameter. It is widely used in regression analysis and was first employed to deal with combustion chemistry concentrations in the previous literature [47]. BCT monotonically projects the mass fractions within $[0, 1]$ to $[-1/\lambda, 0]$ if $\lambda > 0$, and converts the low-order concentrations 10^{-k} to $\mathcal{O}(1)$ magnitude, avoiding the singularity and perturbation sensitivity when approaching zero compared with the logarithm function. Hence, we adopt BCT as a data pre-processing method with $\lambda = 0.1$. In this study, we only apply BCT to species mass fractions due to their inherent multi-scale distribution. For other physical quantities such as temperature and density, BCT pre-processing is deemed unnecessary. Following the BCT transformation of mass fractions, we implement Z-score normalization (i.e., subtract the mean and divide by the standard deviation) across all input and label the dataset to enhance the convergence speed of DNNs.

3.2. Data Generation and Sampling

In general, the performance of DNN training and prediction depends largely on the "data quality", which typically refers to the ability of training data to represent the situations in actual applications. One common practice in improving data quality is to directly sample the data of reactions from reacting hydrodynamic simulations. However, for complex flame simulations, the computational cost becomes prohibitive, especially in three-dimensional cases involving multiple components. Apart from this, the training dataset originates from specific flame configurations, and the corresponding DNN models could only be deployed into

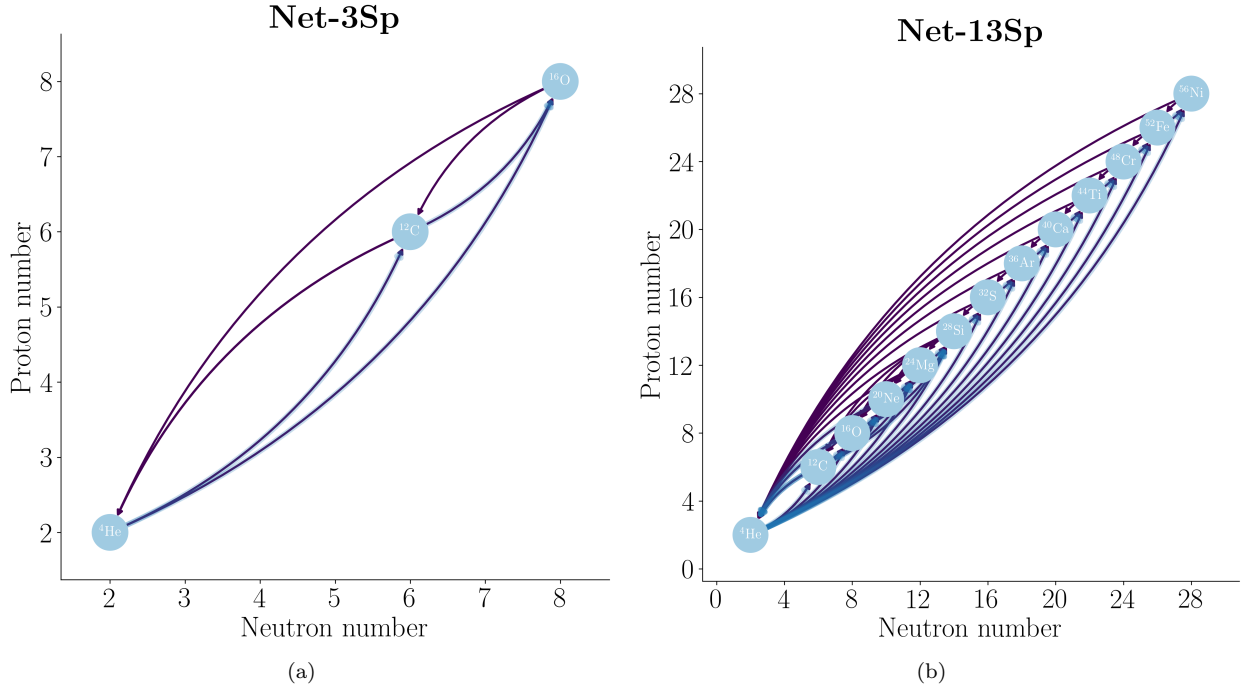


Figure 1. The reaction diagrams of two nuclear reaction networks, both generated by pynucastro, with the arrows for exothermic reactions marked in blue. (a) Reaction schematic of the Net-3Sp, includes two forward reactions and two reverse reactions. (b) Reaction schematic of the Net-13Sp, includes sixteen forward reactions and sixteen reverse reactions.

similar simulation settings, thereby limiting the applicability. This is because the simulation data represents low-dimensional manifolds in the whole thermo-concentration space. The DNNs are capable of learning the features within this manifold distribution, while they perform poorly on the test samples deviating from it. Such a phenomenon has been observed in the previous work of Fan et al. [10]. To address these challenges, we need a sampling method that enhances model generalization capability, enables effective deployment of a single trained model across diverse testing scenarios, and maintains high prediction accuracy.

Compared to chemical reactions, nuclear reactions exhibit significantly greater stiffness and heightened temperature sensitivity. This characteristic not only necessitates the collection of more extensive data from stiff regions, but also results in substantially smaller time scales for intense reaction dynamics, thereby compounding data acquisition challenges. To overcome these issues, we extend the Evolutionary Monte Carlo Sampling (EMCS) [45] for collecting samples from the broad phase space and enhance data acquisition in highly rigid regions. This method is performed independently of hydrodynamics simulations, relying solely on the nuclear ODE solver. The sampling procedure can be easily implemented in the code. The method comprises three main steps:

1. *Range estimation:* Initially, we estimate the sampling ranges for temperature T , density ρ , and species mass fractions X_k based on white dwarf deflagration scenarios.
2. *Monte Carlo sampling:* We conduct Monte Carlo sampling for T , ρ and X_k within the specified value ranges. Notably, mass fractions are randomly sampled on a logarithmic scale, resulting in the formation of the state vector $\mathbf{x}_0(t) = [T, \rho, \mathbf{X}]$.
3. *Data augmentation:* Using each state vector $\mathbf{x}_0(t)$ as an initial value for ODEs, we evolve the system along the ODE trajectory and collect data on it at the time points $[\tau_1, \tau_2, \dots, \tau_n]$, namely $\mathbf{x}_i := \mathbf{x}_{i-1}(t + \tau_i)$, $i = 1, \dots, n$. To better resolve stiff regions, time points are concentrated on the initial reaction stages where reaction stiffness typically peaks. Subsequently, all states \mathbf{x}_i are consolidated to generate the corresponding labeled dataset.

For the two nuclear networks, we configure a one-dimensional pipe with 10000 mesh cells and disable the flow convection module to isolate nuclear reactions. The initial value in each cell is generated by MC method.

The value ranges for $[T, \rho, \mathbf{X}]$, time points of sampling τ and label time Δt for two networks are shown in Table 1. This process runs 500 times to generate a sufficient dataset. For each network, this process yields nearly 100

Table 1. Variable ranges and label time for two networks

Variables	Net-3Sp	Net-13Sp
$T/(10^9 \text{ K})$	[0.2,8]	[1,8]
$\rho/(10^6 \text{ g cm}^{-3})$	[2.5,100]	[20,200]
X_k	$[10^{-6},1]$	$[10^{-10},1]$
$\Delta t/s$	10^{-6}	10^{-7}

NOTE—See also §3.2.

million individual data points. The data are extracted from Castro output files by using yt interface [38]. To ensure the dataset is suitable for training purposes, a filtering process is applied based on the temperature gradient. The rationale behind this filtering is to prioritize data with larger temperature gradients, as these regions are often more challenging for modeling nuclear reactions.

To preserve a greater number of samples from stiff regions, we implement temperature gradient-based filtering during the selection process. For Net-3Sp, 75% of data points with temperature gradients exceeding 10^{13} K s^{-1} are retained, whereas only 8% retention occurs for gradients below this threshold. In contrast, Net-13Sp demonstrate complete retention (100%) for temperature gradients surpassing $8 \times 10^{13} \text{ K s}^{-1}$, with a sharp decline to 10% retention rate for sub-critical gradient conditions. Finally, we obtain approximately 17 million data points for Net-3Sp (see Figure 2(a)) and 28 million data points for Net-13Sp (see Figure 2(b)), as shown in the figure, the sampling range essentially encompasses the data coming from the calibration simulations in §4.

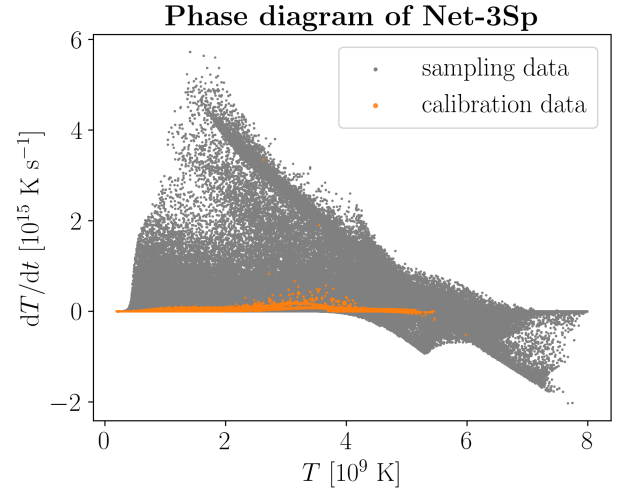
The sampling process is implemented in the Castro hydrodynamics code [51; 1; 2; 34], which is built upon the Starkiller Microphysics libraries [3], and the AMReX framework [49; 33]. The default ODE solver is VODE.

3.3. Training

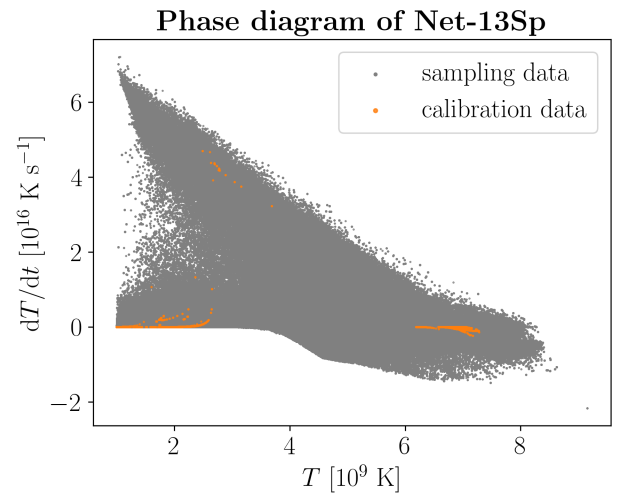
In order to perform training, the data is split into two subsets: 90% for the training set and 10% for the validation set. The validation set is exclusively used to evaluate the model’s performance and does not participate in the training process.

The loss function is set as mean absolute error (i.e. L_1 loss), defined as

$$L_{\text{data}} = \frac{1}{N} \sum_{i=1}^N \|\mathbf{u}_i - \tilde{\mathbf{u}}_i\|_{L_1}, \quad (9)$$



(a)



(b)

Figure 2. The phase diagrams of two nuclear reaction networks illustrate the temperature gradient (ordinate) against the temperature (abscissa). Gray points represent sampling data, while orange points are part of the calibrations data in §4. (a) Phase diagram of the Net-3Sp. (b) Phase diagram of the Net-13Sp.

where $\tilde{\mathbf{u}}_i$ is the prediction with the input being \mathbf{x}_i and N is the training data size. Otherwise, the predicted mass fractions are expected to satisfy the physical constraint: $\sum_k \tilde{X}_k = 1$, and hence the corresponding loss is

$$L_{\text{sum}} = \frac{1}{N} \sum_{i=1}^N \left\| \sum_k \tilde{X}_k^i - 1 \right\|_{L_1}. \quad (10)$$

The total loss for consideration will be

$$L_{\text{all}} = L_{\text{data}} + L_{\text{sum}} \quad (11)$$

and the Adam algorithm is utilized for parameter optimization during the training procedure. The initial

learning rate and batch size are 10^{-4} and 1024, respectively. After training for 2500 epochs, the learning rate is decayed by a factor of 10, and the batch size is increased by 128 times, continuing until reaching 5000 epochs. This two-stage training strategy is designed to enhance the generalization ability of the DNN in the first stage and accelerate convergence in the second stage. In the actual training process, we use PyTorch [28].

As a result, in Figure (3), after 2500 epochs, both the training loss and the validation loss exhibits gradual convergence to less than 10^{-3} for Net-3Sp and less than 10^{-2} for Net-13Sp. And the close alignment between training and validation losses indicates the sufficiency of our dataset for training. Finally, trained neural networks are selected based on the number of epochs that yield optimal performance: 2600 epochs for Net-3Sp and 4000 epochs for Net-13Sp.

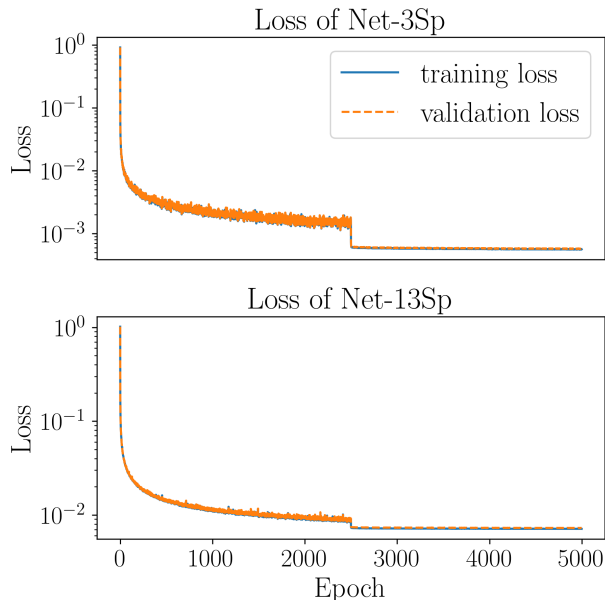


Figure 3. L1 loss of two nuclear reaction networks, each training session consisted of 5000 epochs. The top panel is the loss of Net-3Sp. The bottom panel is the loss of Net-13Sp.

4. CALIBRATION RESULTS

To verify the accuracy of the neural network, we perform calibrations in zero-dimensional, one-dimensional, and two-dimensional scenarios. For one-dimensional and two-dimensional calibration, we integrate the neural network into Kratos [39] using PyTorch [28], then simulate and calibrate using both the neural network and the direction integration. Kratos is a newly developed astrophysical fluid dynamics code optimized for heterogeneous computing architectures. Kratos provides a scalable, high-performance computational framework

Table 2. Initial conditions of zero-dimensional calibrations for Net-3Sp

Variables	Calibration I (Figure 5(a))	Calibration II (Figure 5(b))
$T/(10^8 \text{ K})$	4	4.5
$\rho/(10^6 \text{ g cm}^{-3})$	2	1.1
$X(^4\text{He})$	0.6	0.4
$X(^{12}\text{C})$	0.2	0.3
$X(^{16}\text{O})$	0.2	0.3

for complex simulations, emphasizing graphics processing unit (GPU) efficiency and modular extensibility. Alternatively, with the help of the HIP-CPU⁷ library, Kratos can be easily deployed on CPU architectures. To resolve compressible reacting flows, Kratos implements a finite-volume Godunov method, and involves its own nuclear reaction models to calibrate the reactions against. The numerical scheme combines Piecewise Linear Method (PLM) spatial reconstruction with HLLC Riemann solvers, providing second-order accuracy while preserving positivity for multi-species systems. In addition, Kratos framework also includes a thermochemistry module [40], which is adapted for thermonuclear reactions in order to provide independent benchmarks for us to compare and verify the evolution results using DeePODE.

4.1. Zero-dimensional calibration

This section details zero-dimensional multi-step calibration for two networks, with extended multi-point single-step verification relegated to Appendix A. For Net-3Sp, we conduct simulations using two different sets of initial parameters, each run for 2,000 time steps. The initial temperatures, densities, and mass fractions of $\{^4\text{He}, ^{12}\text{C}, ^{16}\text{O}\}$ for the two simulations are shown in Table 2.

The simulation results are presented in Figure 4. In Figure 4(a), we observe that the results obtained from the neural network closely match those from the direction integration, with minimal differences. In Figure 4(b), the results show only a slight inaccuracy in regions with high rigidity, while the rest of the results align very well with expectations. This minor discrepancy may arise from limitations described by the frequency principle [27]. However, this deviation has a negligible influence on the subsequent equilibrium state.

⁷ <https://github.com/ROCM/HIP-CPU>

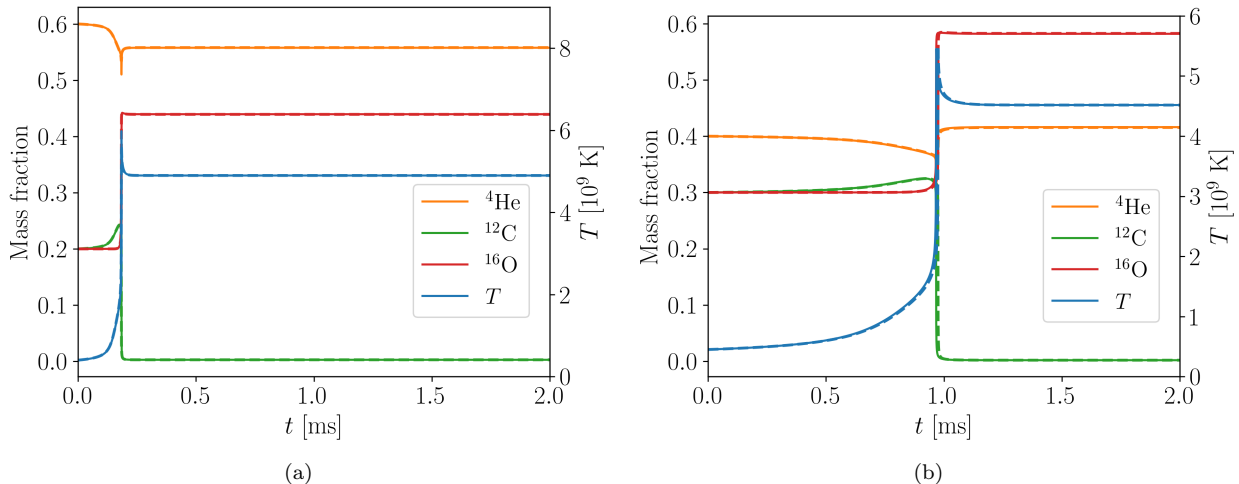


Figure 4. Two zero-dimensional calibrations for Net-3Sp. We compare the temperature and mass fractions of various isotopes between neural network solutions (dashed lines) and direction integration solutions (solid lines) in simulations of 2 ms each. (a) Zero-dimensional calibration I for Net-3Sp. (b) Zero-dimensional calibration II for Net-3Sp.

For Net-13Sp, we perform simulations with two distinct sets of initial parameters, each run for 1,000 time steps. The initial parameters for the first case are randomly generated. For the second case, the parameters are derived from the conditions of internal deflagration in white dwarfs [18], with the following values: an initial temperature of 2×10^9 K, an initial density of 1×10^8 g cm $^{-3}$, and an initial isotope composition consisting of approximately 50% ^{12}C and 50% ^{16}O . The results, shown in Figure 5, indicate that, apart from minor deviations in the mass fractions of certain isotopes during the steps of high rigidity, the overall agreement between the neural network and the direction integration is excellent.

4.2. One-dimensional calibration

For the one-dimensional calibration of Net-3Sp, we adopt parameter settings corresponding to surface combustion on white dwarfs during the double detonation process described by Rivas et al. [29]. The spatial domain of the simulation spans $x/(10^3 \text{ m}) \in [-6.144, 6.144]$ with 256 grid cells and the boundary conditions are outflow. The background conditions are as follows: temperature $T_0 = 2 \times 10^8$ K, density $\rho_0 = 1 \times 10^7$ g cm $^{-3}$. To initiate the simulation, the temperature in the central region is increased while maintaining constant pressure. The new temperature is defined as:

$$T = \frac{3T_0}{2} + \frac{T_0}{2} \tanh\left(4 - \frac{|x|}{r'}\right), \quad (12)$$

where x represents the position of the grid cells, and $r' = 1.536 \times 10^2$ m. The simulation runs for 1.5 ms. As shown in Figure 6(a), the central region ignites after being preheated and subsequently propagates out-

ward in both directions. The results, presented in Figure 7(b), demonstrate excellent agreement between the neural network and the direction integration, with only minor deviations in the mass fraction observed in a few grid cells.

For Net-13Sp, we utilize parameter configurations representative of internal deflagration in white dwarfs, following the work of Hristov et al. [18]. The spatial domain of the simulation is $x/(10^2 \text{ m}) \in [-3.072, 3.072]$ with 256 grid cells, the boundary conditions are also outflow. The background conditions are as follows: temperature $T_0 = 10^9$ K, density $\rho_0 = 10^8$ g cm $^{-3}$ and the initial isotope composition consists of approximately 50% ^{12}C and 50% ^{16}O . As with Net-3Sp, a controlled thermal perturbation is imposed within the center domain while maintaining constant pressure. The temperature distribution is the same as Equation 12 but with $r' = 15.36$ m. And this simulation runs for 20 μs .

Figure 7(a) shows the preheated core igniting with bidirectional flame propagation, the same as Figure 6(a). The results, illustrated in Figure 7(b), show that when the simulation uses the neural network entirely (DNN-1), the reacted region exhibits small deviation compared to the direction integration, and oscillations are observed. This indicates limitations in the neural network's accuracy near the reaction equilibrium region. Consequently, we set the upper temperature limit of the neural network to 6.5×10^9 K (DNN-2), where the computational results exhibit close alignment with direct numerical integration. Under these operational conditions, the neural network's computational utilization rate is maintained above 88%, demonstrating its efficiency. This strategy can be useful in practice, since

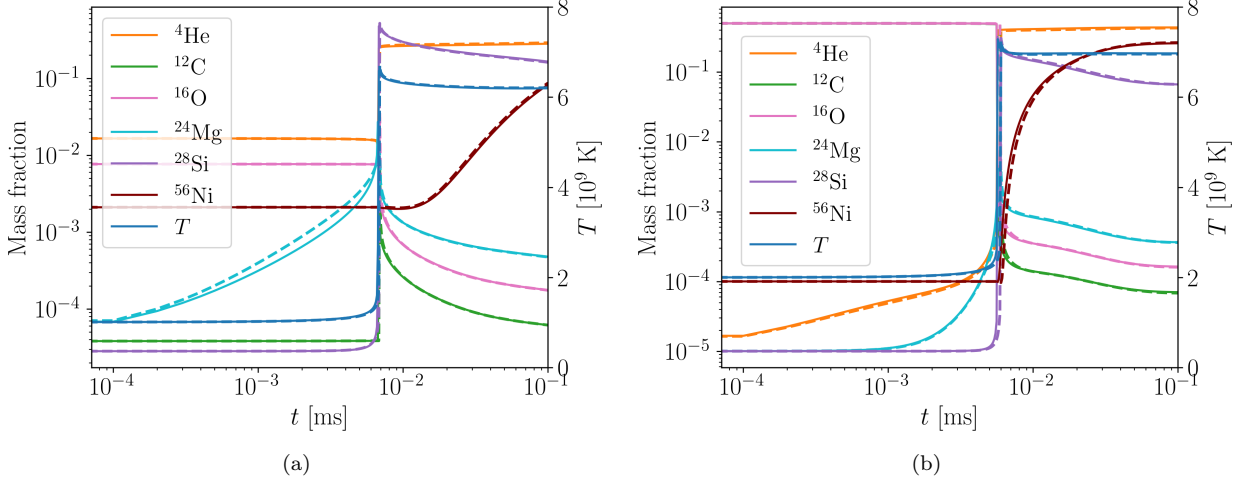


Figure 5. Two zero-dimensional calibration for Net-13Sp. We compare the temperature and mass fractions of various isotopes between neural network solutions (dashed lines) and direction integration solutions (solid lines) in simulations of 0.1 ms each. (a) Zero-dimensional calibration I for Net-13Sp. (b) Zero-dimensional calibration II for Net-13Sp.

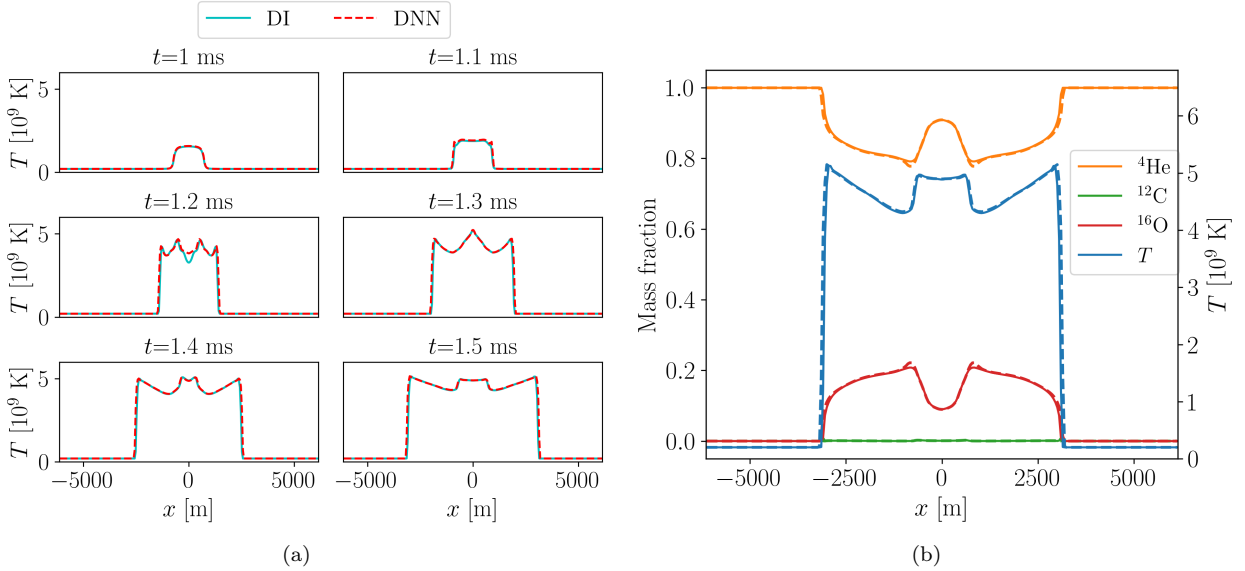


Figure 6. The one-dimensional simulation of Net-3Sp. (a) The temperature change diagram of the one-dimensional case. (b) Comparison of temperature and mass fractions of isotopes obtained from simulations using neural networks (dashed lines) and direction integration (solid lines) at $t = 1.5$ ms.

direct integration is deemed sufficient for treating the equilibrium region, while the neural network tends to outperform in stiffer ones.

4.3. Two-dimensional calibration

The first two-dimensional calibration for Net-3Sp extends the one-dimensional setup to a two-dimensional spatial domain: $x/(10^3 \text{ m}) \in [-6.144, 6.144]$, $y/(10^3 \text{ m}) \in [-6.144, 6.144]$ with a grid resolution of 256×256 cells, the boundary conditions in the x and y directions are both outflow. The background conditions are defined as follows: temperature $T_0 = 2 \times 10^8 \text{ K}$, den-

sity $\rho_0 = 1 \times 10^7 \text{ g cm}^{-3}$, and isotopic composition is almost entirely composed of ^4He . The perturbation configuration retains structural consistency with the one-dimensional calibration (12), with the spatial coordinate systematically substituted from x to $R = \sqrt{x^2 + y^2}$, and $r' = 3.072 \times 10^2 \text{ m}$. This simulation also runs for 1.5 ms.

After the simulation, the results are analyzed by extracting data points along the line $y = 0$ for comparison. As shown in the Figure 8, the temperature and density profiles, as well as the mass fractions, align closely with those obtained using the direction integration. Devia-

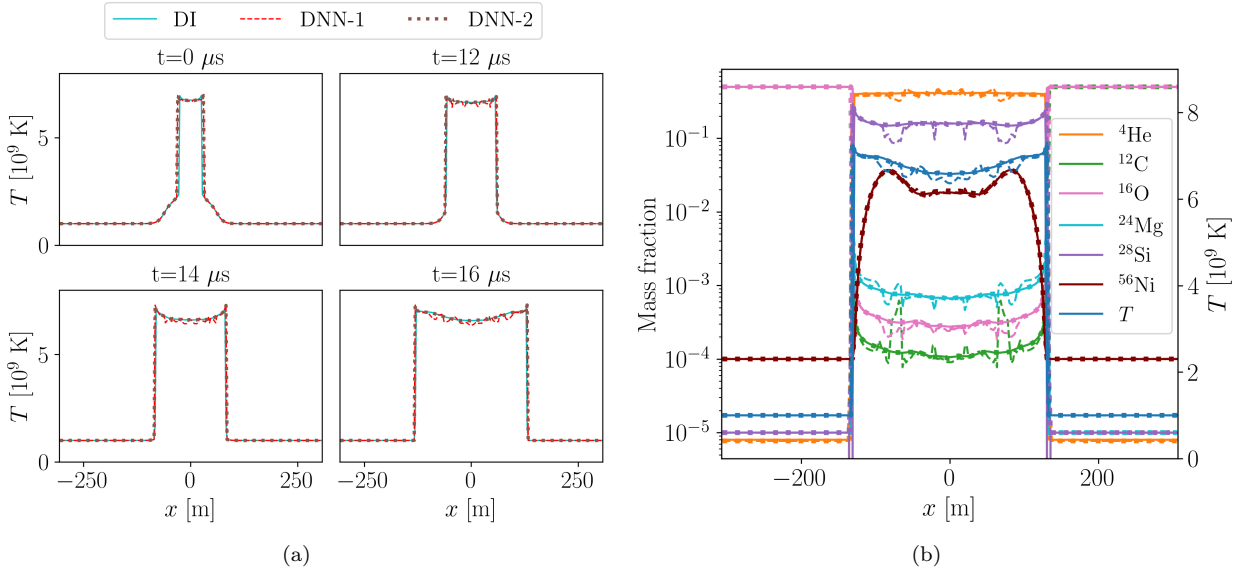


Figure 7. The one-dimensional simulation of Net-13Sp. (a) The temperature change diagram of the one-dimensional case. (b) Comparison of temperature and mass fractions of isotopes obtained from simulations using DNN-1 (dashed lines), DNN-2 (dotted lines) and direction integration (solid lines) at $t = 20 \mu\text{s}$.

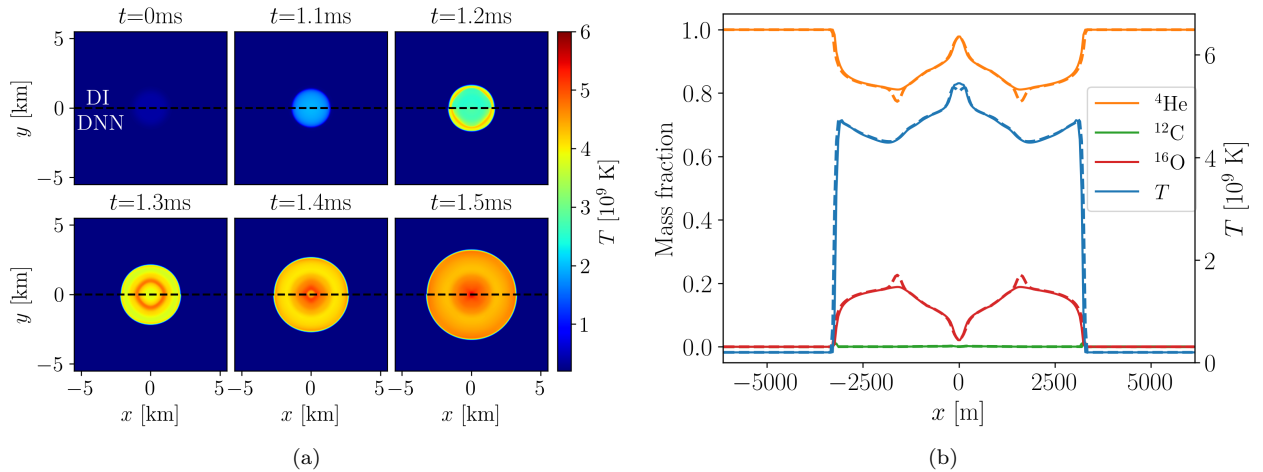


Figure 8. Two-dimensional simulations using Net-3Sp. (a) The upper and lower halves of the subplots show the temperature evolution from the direction integration and the neural network, respectively. (b) Comparisons of the temperature and mass fractions of isotopes obtained from simulations using the neural network (dashed lines) and the direct integration (solid lines) at $t = 1.5\text{ms}$ along the $y = 0$ axis.

tions are observed in the mass fractions for only a small number of grid cells, similar to the one-dimensional calibration results. These discrepancies are minimal and do not significantly affect the overall accuracy of the simulation.

The second two-dimensional calibration for Net-3Sp is the Kelvin-Helmholtz instabilities case, which is motivated by and adapted from Casanova et al. [6]. The spatial domain is defined as: $x/(10^3 \text{ m}) \in [-1.2288, 1.2288]$, $y/(10^2 \text{ m}) \in [-6.144, 6.144]$ with a grid resolution of 512×256 cells. The x -boundary conditions are periodic,

while the y -boundary conditions are reflecting. The ini-

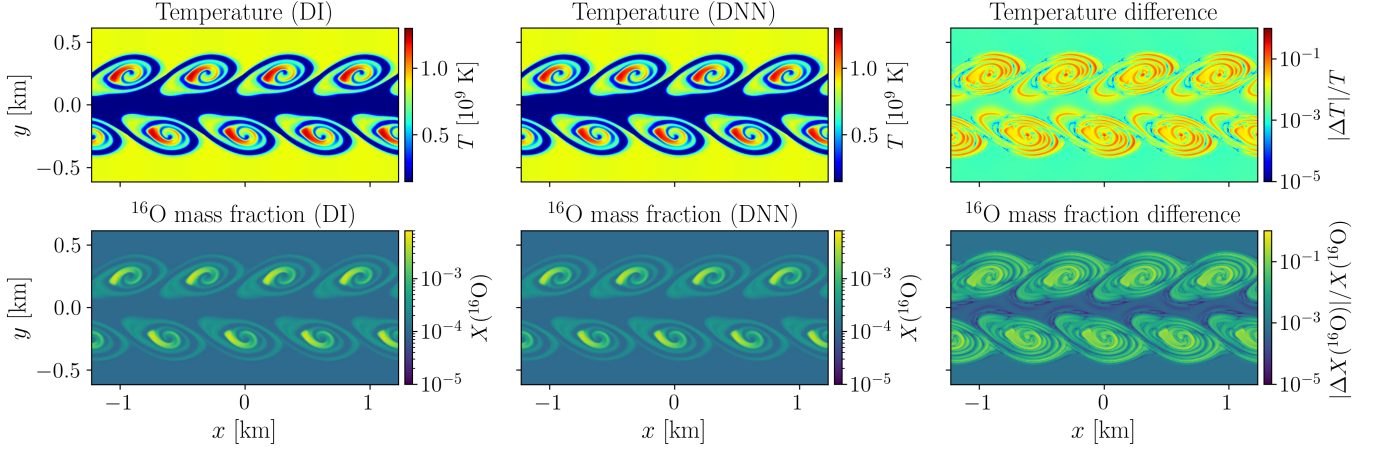


Figure 9. The Kelvin-Helmholtz instability tests results, comparing the temperature (upper row) and mass fraction of O16 (lower row) at $t = 6.5$ ms from the direction integration (left column) and the DNN (middle column) results. The right column shows the relative difference.

tial conditions are set as:

$$\rho = \rho_0 + \delta\rho \tanh\left(\frac{y_0 - |y|}{L}\right), \quad (13)$$

$$v_x = v_{x0} \tanh\left(\frac{y_0 - |y|}{L}\right), \quad (14)$$

$$v_y = v_{y0} \cos\left(\frac{2\pi}{\lambda}\right) \exp\left[-\frac{(|y| - y_0)^2}{2y_0^2}\right], \quad (15)$$

$$X(^4\text{He}) = X_0 + \frac{1 - 3X_0}{2} \left[1 + \tanh\left(\frac{y_0 - |y|}{L}\right)\right], \quad (16)$$

$$X(^{12}\text{C}) = X_0 + \frac{1 - 3X_0}{2} \left[1 - \tanh\left(\frac{y_0 - |y|}{L}\right)\right], \quad (17)$$

$$X(^{16}\text{O}) = X_0, \quad (18)$$

where ρ_0 , X_0 , v_{x0} and v_{y0} are the reference values for density, mass fraction and x , y velocity components, $\delta\rho$ is the difference in density across the shearing layer with thickness L , λ is the velocity perturbation wavelength. Here, $\rho_0 = 1.5 \times 10^7 \text{ g cm}^{-3}$, $\delta\rho = 4.5 \times 10^6 \text{ g cm}^{-3}$, $y_0 = 2.048 \times 10^2 \text{ m}$, $L = 30.72 \text{ m}$, $v_{x0} = -2 \times 10^7 \text{ cm s}^{-1}$, $v_{y0} = 2 \times 10^6 \text{ cm s}^{-1}$, $\lambda = 6.144 \times 10^2 \text{ m}$, $X_0 = 10^{-4}$.

The results are shown in Figure 9, which compares the temperature and the mass fraction of ^{16}O at $t = 6.5$ ms. As evidenced by the figure, both temperature profiles and ^{16}O mass fractions exhibit minimal variations, demonstrating maximum relative errors within approximately 20%. The observed discrepancies are predominantly localized near the flow boundary regions, potentially attributable to minor structural displacements during the transport processes.

For the two-dimensional calibration of Net-13Sp, we employ a V-shaped flame configuration (Figures 10, 11), which also utilizes parameter configurations de-

rived from Hristov et al. [18]. The spatial domain is defined as: $x/(10^2 \text{ m}) \in [-9.216, 3.072]$, $y/(10^2 \text{ m}) \in [-3.072, 3.072]$ with a grid resolution of 512×256 cells, the x-boundary conditions are outflow and reflect, the y-boundary conditions are periodic. The initial conditions are as follows:

- Upstream: $T = 2 \times 10^9 \text{ K}$, $\rho = 5 \times 10^7 \text{ g cm}^{-3}$
- Downstream: $T = 1 \times 10^9 \text{ K}$, $\rho = 1 \times 10^8 \text{ g cm}^{-3}$
- Isotopic composition (both regions): approximately 50% ^{12}C and 50% ^{16}O .

This simulation runs for $40 \mu\text{s}$. During the simulation, the flame on the right ignites after preheating and propagates towards the left, as shown in Figure 10. Same as the 1D calibration, two simulations are performed: full adoption of the neural network (DNN-1) and temperature-limited adoption below $6.5 \times 10^9 \text{ K}$ (DNN-2), with identical grid parameters. After the simulations, data points along the line $y = 0$ are extracted for comparison. As demonstrated in Figure 11, when the neural network operates continuously (DNN-1) during the simulation, the reaction zone exhibits minor deviations accompanied by pronounced oscillations. However, implementing a temperature activation threshold (DNN-2) for the network yields results that demonstrate strong agreement with direct integration values. This adjustment significantly improves stability while preserving accuracy, and the network operates at 76% utilization under thermal gating.

4.4. Computational time cost comparison

While GPU architectures are generally considered more suitable for neural network acceleration due to

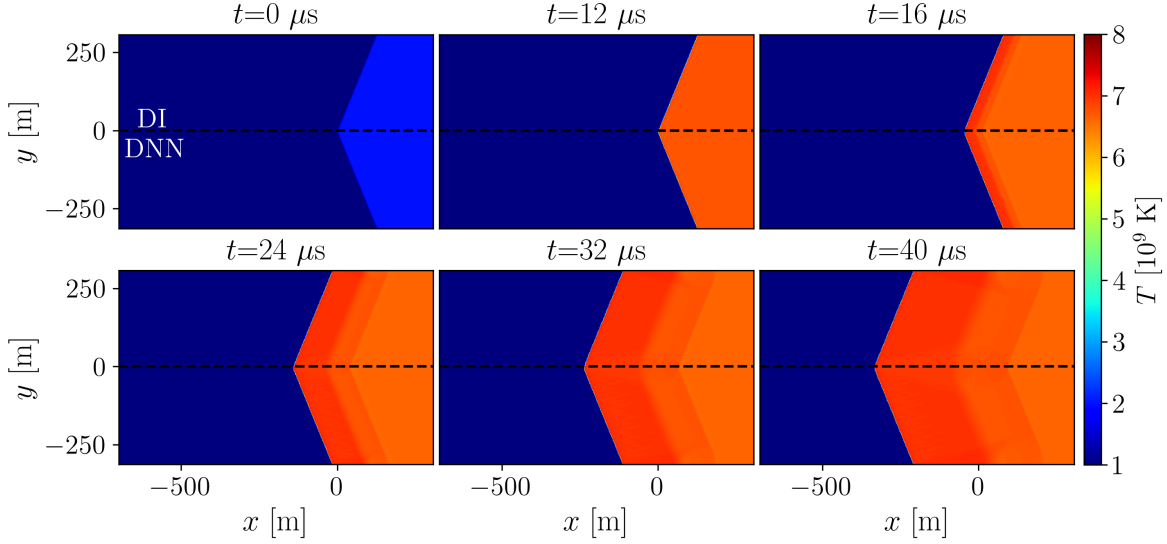


Figure 10. The temperature change diagram of the two-dimensional case for Net-13Sp. The upper part of the subplot in each step shows the direction integration results, and the lower part shows the neural network results.

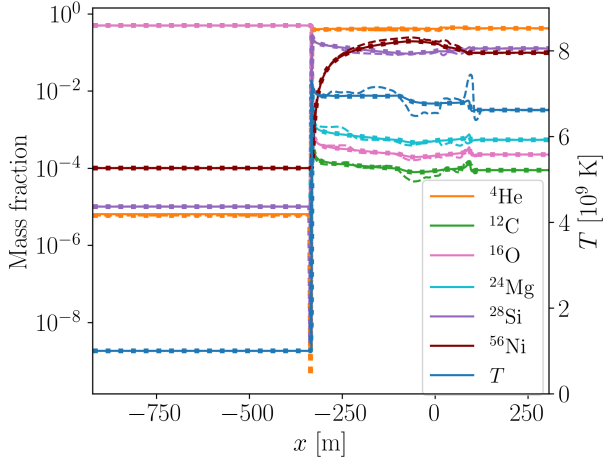


Figure 11. Comparison of temperature and mass fractions of isotopes obtained from two-dimensional simulations of Net-13Sp using DNN-1 (dashed lines), DNN-2 (dotted lines) and direction integration (solid lines) at $t = 40 \mu\text{s}$ along the x axis where $y = 0$.

their massive parallel computing capabilities, our current implementation focuses on CPU-based validation as a crucial first step benchmark. Experimental results demonstrate that our neural network integration achieves $\sim 2.59\times$ and $\sim 2.57\times$ (4.4) speedup for 13-species simulations in 1D (Figure 7) and 2D (Figures 10, 11) configurations respectively, when executed on a six-core Intel i5-12400F CPU processor.

Notably, these CPU-based acceleration metrics should be interpreted as conservative estimates of the method’s potential. The intrinsic parallelism of neural network

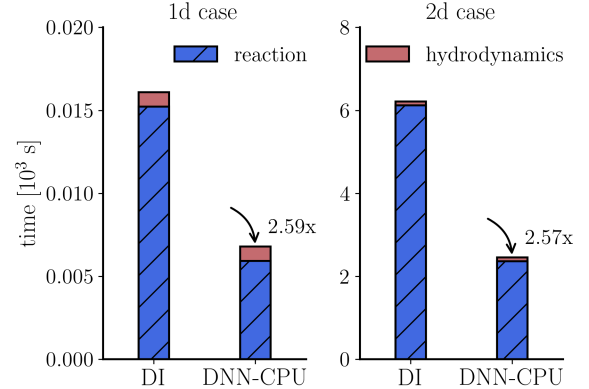


Figure 12. The comparison of computation time between solving nuclear reactions using neural networks and direction integration. The left panel shows the one-dimensional case, while the right panel shows the two-dimensional case.

computations remains fundamentally constrained by CPU architectures’ limited thread scalability and memory bandwidth. To fully exploit the algorithm’s acceleration capacity, our ongoing work involves integrating the neural network component directly into the GPU software architecture, rather than leveraging PyTorch for CPU-side invocation. This migration is expected to i) establish more realistic acceleration baselines through explicit comparison of CPU/GPU computational graphs, and ii) leverage GPU tensor cores’ mixed-precision computing to further optimize the inference latency-critical components.

5. SUMMARY AND FUTURE WORKS

This work demonstrates the successful development and validation of deep neural network (DNN) surrogate models for accelerating astrophysical nuclear reaction simulations. By leveraging the DeePODE framework, we established a surrogate models for both 3-species and 13-species reaction networks (Net-3Sp and Net-13Sp), achieving comparable accuracy to direct integration while attaining a $\sim 2.6\times$ speedup on CPU architectures. The models generalize robustly, across zero-dimensional calculations (temporal evolution at one spatial point) through two-dimensional simulations, via the temperature-thresholded deployment strategies, maintaining neural network utilization rates above 75% in multi-dimensional scenarios. With the evolutionary Monte Carlo sampling (EMCS) employed for broad-phase-space data generation, and Box-Cox transformations that handle multi-scale mass fractions, the DeePODE module perform fast and accurate predictions within the hybrid integration paradigm, dynamically balancing the capability of DNN predictions in stiff regions with traditional solvers adopted elsewhere. Validation across flame propagation, Kelvin-Helmholtz instabilities, and white dwarf deflagration scenarios confirm the framework’s ability to resolve complex reacting flows, while accelerating the overall computation by circumventing stiffness limitations inherent to conventional ODE solvers.

While this paper establishes a foundation for data-driven modeling of nuclear reacting flows, several critical advancements remain to fully realize the potential of DNN surrogates in astrophysical simulations. One possibility is implementing on-the-fly training, where the neural network is dynamically trained and updated during the initial stages of a simulation. This paradigm would reduce the need for precomputed datasets by integrating real-time data generation and model refinement into the simulation workflow. Expanding the scope to larger reaction networks (e.g. ~ 100 species) and multi-physics couplings could also be promising in implementing these data-driven methods in extreme regimes with higher complications. Coupling DNN surrogates with regression methods could yield interpretable, reduced-order models for nucleosynthesis pathways, bridging machine learning with theoretical nuclear astrophysics. These advancements could collectively enable high-fidelity, end-to-end simulations of multi-scale astrophysical phenomena, while overcoming the computational barriers imposed by conventional stiff solvers.

ACKNOWLEDGMENTS

This work is supported by the National Natural Science Foundation of China under Grants No. 92270001 (Z. X.), 12371511 (Z. X.), 12422119 (Z. X.), 92470127 (T. Z.), and 12305246 (Y. Z.).

APPENDIX

A. SINGLE-STEP TESTS WITH ZERO SPATIAL DIMENSIONS

We conduct a large number of zero-dimensional single-step tests and compare the results with those of direction integration. The method of data collection is similar to sampling, but these test data are not included in the training set. Approximately 5×10^5 sets of data are used in the testing of Net-3Sp, and approximately 1 million sets of data are used in the testing of Net-13Sp. From Figure 13 and Figure 14, it can be seen that there are only a few prediction values with deviations, while other predictions are very accurate.

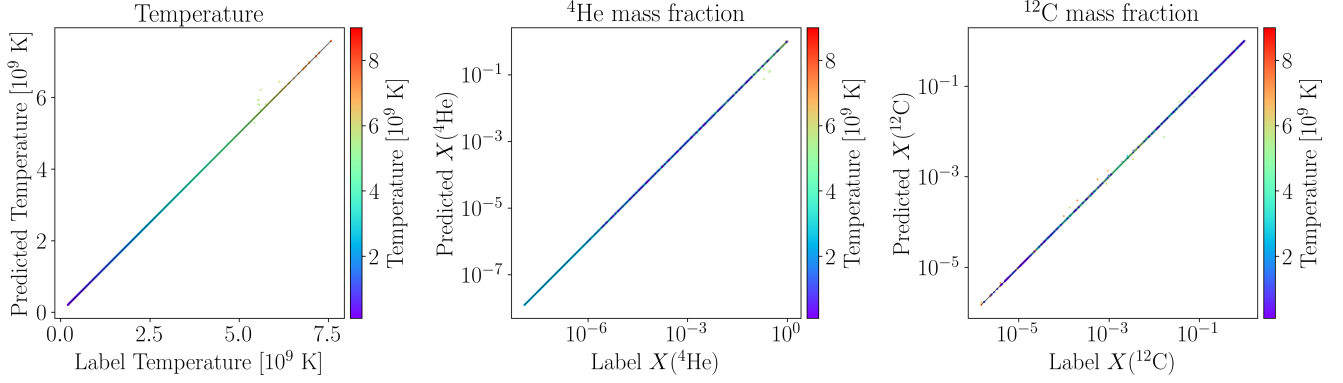


Figure 13. One step tests for Net-3Sp. The horizontal and vertical axes represent the results of one step predicted by the direction integration and the neural network, respectively.

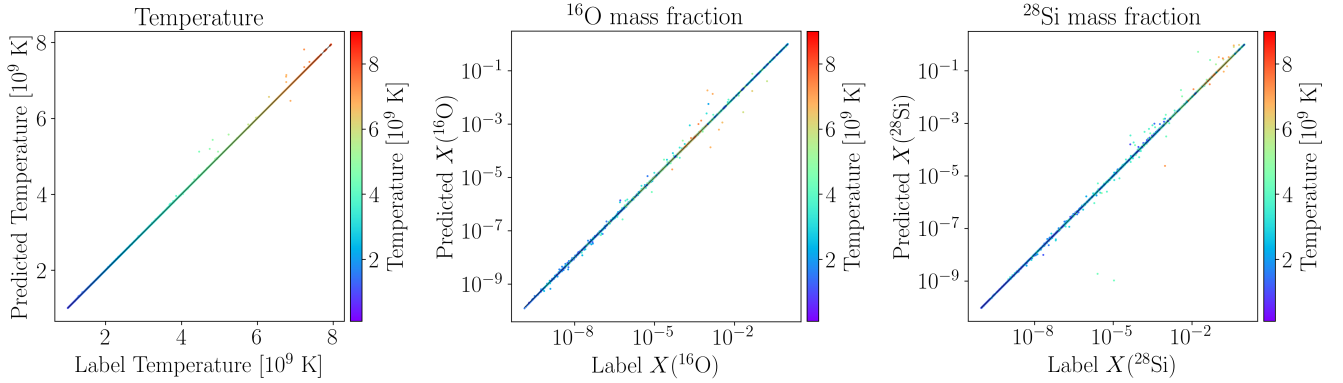


Figure 14. One step tests for Net-13Sp. The horizontal and vertical axes represent the results of one step predicted by the direction integration and the neural network, respectively.

REFERENCES

REFERENCES

- [1]Almgren, A., Sazo, M. B., Bell, J., et al. 2020, Journal of Open Source Software, 5, 2513, doi: [10.21105/joss.02513](https://doi.org/10.21105/joss.02513)
- [2]Almgren, A. S., Beckner, V. E., Bell, J. B., et al. 2010, ApJ, 715, 1221, doi: [10.1088/0004-637X/715/2/1221](https://doi.org/10.1088/0004-637X/715/2/1221)
- [3]AMReX-Astro Microphysics Development Team, Bishop, A., Fields, C. E., et al. 2025, AMReX-Astro/Microphysics: Release 25.01, 25.01, Zenodo, doi: [10.5281/zenodo.14584895](https://doi.org/10.5281/zenodo.14584895)
- [4]Boehnlein, A., Diefenthaler, M., Fanelli, C., et al. 2022, Reviews of Modern Physics, 94, 31003, doi: [10.1103/RevModPhys.94.031003](https://doi.org/10.1103/RevModPhys.94.031003)
- [5]Box, G. E. P., & Cox, D. R. 1964, Journal of the Royal Statistical Society: Series B (Methodological), 26, 211, doi: <https://doi.org/10.1111/j.2517-6161.1964.tb00553.x>
- [6]Casanova, J., José, J., García-Berro, E., Shore, S. N., & Calder, A. C. 2011, Nature, 478, 490, doi: [10.1038/nature10520](https://doi.org/10.1038/nature10520)
- [7]Degraeve, J., Felici, F., Buchli, J., et al. 2022, Nature, 602, 414, doi: [10.1038/s41586-021-04301-9](https://doi.org/10.1038/s41586-021-04301-9)
- [8]Du, P., Parikh, M. H., Fan, X., Liu, X.-Y., & Wang, J.-X. 2024, Nature Communications, 15, 10416, doi: [10.1038/s41467-024-54712-1](https://doi.org/10.1038/s41467-024-54712-1)

- [9]Fan, D., Nonaka, A., Almgren, A. S., Harpole, A., & Zingale, M. 2019, *ApJ*, 887, 212, doi: [10.3847/1538-4357/ab4f75](https://doi.org/10.3847/1538-4357/ab4f75)
- [10]Fan, D., Willcox, D. E., DeGrendele, C., Zingale, M., & Nonaka, A. 2022, *The Astrophysical Journal*, 940, 134, doi: [10.3847/1538-4357/ac9a4b](https://doi.org/10.3847/1538-4357/ac9a4b)
- [11]Fryxell, B., Olson, K., Ricker, P., et al. 2000, *The Astrophysical Journal Supplement Series*, 131, 273, doi: [10.1086/317361](https://doi.org/10.1086/317361)
- [12]Gamezo, V. N., Khokhlov, A. M., & Oran, E. S. 2004, *Physical Review Letters*, 92, 211102, doi: [10.1103/PhysRevLett.92.211102](https://doi.org/10.1103/PhysRevLett.92.211102)
- [13]—. 2005, *The Astrophysical Journal*, 623, 337, doi: [10.1086/428767](https://doi.org/10.1086/428767)
- [14]García-Senz, D., Cabezón, R. M., Arcones, A., Relaño, A., & Thielemann, F. K. 2013, *Monthly Notices of the Royal Astronomical Society*, 436, 3413, doi: [10.1093/mnras/stt1821](https://doi.org/10.1093/mnras/stt1821)
- [15]Ghosh, A., & Kushnir, D. 2022, *Monthly Notices of the Royal Astronomical Society*, 515, 286, doi: [10.1093/mnras/stac1846](https://doi.org/10.1093/mnras/stac1846)
- [16]Gronow, S., Collins, C. E., Sim, S. A., & Roepke, F. K. 2021, *Astronomy & Astrophysics*, 649, A155, doi: [10.1051/0004-6361/202039954](https://doi.org/10.1051/0004-6361/202039954)
- [17]Guichandut, S., Zingale, M., & Cumming, A. 2024, Hydrodynamical simulations of proton ingestion flashes in Type I X-ray Bursts, arXiv. <http://arxiv.org/abs/2405.08952>
- [18]Hristov, B., Collins, D. C., Hoefflich, P., Weatherford, C. A., & Diamond, T. R. 2018, *The Astrophysical Journal*, 858, 13, doi: [10.3847/1538-4357/aab7f2](https://doi.org/10.3847/1538-4357/aab7f2)
- [19]Huerta, E. A., Allen, G., Andreoni, I., et al. 2019, *Nature Reviews Physics*, 1, 600, doi: [10.1038/s42254-019-0097-4](https://doi.org/10.1038/s42254-019-0097-4)
- [20]Ihme, M., Chung, W. T., & Mishra, A. A. 2022, *Progress in Energy and Combustion Science*, 91, 101010
- [21]Johnson, E. T., & Zingale, M. 2024, Simulating Lateral H/He Flame Propagation in Type I X-ray Bursts, arXiv. <https://arxiv.org/abs/2402.02013>
- [22]Jumper, J., Evans, R., Pritzl, A., et al. 2021, *Nature*, 596, 583, doi: [10.1038/s41586-021-03819-2](https://doi.org/10.1038/s41586-021-03819-2)
- [23]Kičičić, I., Vlachas, P. R., Arampatzis, G., et al. 2023, *Computer Methods in Applied Mechanics and Engineering*, 415, 116204, doi: [10.1016/j.cma.2023.116204](https://doi.org/10.1016/j.cma.2023.116204)
- [24]Kochkov, D., Smith, J. A., Alieva, A., et al. 2021, *Proceedings of the National Academy of Sciences*, 118, e2101784118, doi: [10.1073/pnas.2101784118](https://doi.org/10.1073/pnas.2101784118)
- [25]Kumar, A., & Echehki, T. 2024, *Fuel*, 365, 131212, doi: [10.1016/j.fuel.2024.131212](https://doi.org/10.1016/j.fuel.2024.131212)
- [26]Kushnir, D., Katz, B., Dong, S., Livne, E., & Fernández, R. 2013, *The Astrophysical Journal*, 778, L37, doi: [10.1088/2041-8205/778/2/L37](https://doi.org/10.1088/2041-8205/778/2/L37)
- [27]Luo, T., Ma, Z., Xu, Z.-Q. J., & Zhang, Y. 2019, Theory of the Frequency Principle for General Deep Neural Networks, arXiv, doi: [10.48550/arXiv.1906.09235](https://doi.org/10.48550/arXiv.1906.09235)
- [28]Paszke, A., Gross, S., Massa, F., et al. 2019, in *Advances in Neural Information Processing Systems* 32, ed. H. Wallach, H. Larochelle, A. Beygelzimer, F. d'Alché-Buc, E. Fox, & R. Garnett (Curran Associates, Inc.), 8024–8035. <http://papers.neurips.cc/paper/9015-pytorch-an-imperative-style-high-performance-deep-learning-library.pdf>
- [29]Rivas, F., Harris, J. A., Hix, W. R., & Messer, O. E. B. 2022, *The Astrophysical Journal*, 937, 2, doi: [10.3847/1538-4357/ac8b06](https://doi.org/10.3847/1538-4357/ac8b06)
- [30]Smith, A. I., Johnson, E. T., Chen, Z., et al. 2023, *The Astrophysical Journal*, 947, 65, doi: [10.3847/1538-4357/acbaff](https://doi.org/10.3847/1538-4357/acbaff)
- [31]Strang, G. 1968, *SIAM Journal on Numerical Analysis*, 5, 506, doi: [10.1137/0705041](https://doi.org/10.1137/0705041)
- [32]—. 1968, *SIAM Journal on Numerical Analysis*, 5, 506, doi: [10.1137/0705041](https://doi.org/10.1137/0705041)
- [33]the AMReX Development Team, Almgren, A., Beckner, V., et al. 2025, AMReX-Codes/amrex: AMReX 25.01, 25.01, Zenodo, doi: [10.5281/zenodo.14589566](https://doi.org/10.5281/zenodo.14589566)
- [34]the Castro Development Team, Almgren, A., Barrios Sazo, M., et al. 2025, AMReX-Astro/Castro: Release 25.01, 25.01, Zenodo, doi: [10.5281/zenodo.14589933](https://doi.org/10.5281/zenodo.14589933)
- [35]the pynucastro development, Boyd, B., Cao, L., et al. 2024, pynucastro/pynucastro: pynucastro 2.4.0, 2.4.0, Zenodo, doi: [10.5281/zenodo.13899727](https://doi.org/10.5281/zenodo.13899727)
- [36]Townsend, D. M., Miles, B. J., Shen, K. J., & Kasen, D. 2019, *The Astrophysical Journal*, 878, L38, doi: [10.3847/2041-8213/ab27cd](https://doi.org/10.3847/2041-8213/ab27cd)
- [37]Tunyasuvunakool, K., Adler, J., Wu, Z., et al. 2021, *Nature*, 596, 590, doi: [10.1038/s41586-021-03828-1](https://doi.org/10.1038/s41586-021-03828-1)
- [38]Turk, M. J., Smith, B. D., Oishi, J. S., et al. 2011, *The Astrophysical Journal Supplement Series*, 192, 9, doi: [10.1088/0067-0049/192/1/9](https://doi.org/10.1088/0067-0049/192/1/9)
- [39]Wang, L. 2025, *ApJS*, 277, 63, doi: [10.3847/1538-4365/adbdb6](https://doi.org/10.3847/1538-4365/adbdb6)
- [40]—. 2025, arXiv e-prints, arXiv:2504.04941, doi: [10.48550/arXiv.2504.04941](https://doi.org/10.48550/arXiv.2504.04941)
- [41]Wang, T., Yi, Y., Yao, J., et al. 2025, *Combustion and Flame*, 275, 114105

- [42]Weng, Y., Li, H., Zhang, H., Chen, Z. X., & Zhou, D. 2025, *Combustion and Flame*, 272, 113847, doi: [10.1016/j.combustflame.2024.113847](https://doi.org/10.1016/j.combustflame.2024.113847)
- [43]Willcox, D. E., & Zingale, M. 2018, *Journal of Open Source Software*, 3, 588, doi: [10.21105/joss.00588](https://doi.org/10.21105/joss.00588)
- [44]Xu, Z.-Q. J., Yao, J., Yi, Y., et al. 2024, Solving multiscale dynamical systems by deep learning, arXiv. <http://arxiv.org/abs/2401.01220>
- [45]Yao, J., Yi, Y., Hang, L., et al. 2025, Solving Multiscale Dynamical Systems by Deep Learning, arXiv, doi: [10.48550/arXiv.2401.01220](https://doi.org/10.48550/arXiv.2401.01220)
- [46]Zhang, T., Yi, Y., Xu, Y., et al. 2022, *Combustion and Flame*, 245, 112319, doi: [10.1016/j.combustflame.2022.112319](https://doi.org/10.1016/j.combustflame.2022.112319)
- [47]Zhang, T., Zhang, Y., E, W., & Ju, Y. 2021, DLODE: a deep learning-based ODE solver for chemistry kinetics, doi: [10.2514/6.2021-1139](https://doi.org/10.2514/6.2021-1139)
- [48]Zhang, T., Zhang, Y., E, W., & Ju, Y. 2021, in *AIAA Scitech 2021 Forum*, 1139
- [49]Zhang, W., Almgren, A., Beckner, V., et al. 2019, *Journal of Open Source Software*, 4, 1370, doi: [10.21105/joss.01370](https://doi.org/10.21105/joss.01370)
- [50]Zingale, M. 2023, *The Astrophysical Journal*
- [51]Zingale, M., Katz, M. P., Bell, J. B., et al. 2019, *The Astrophysical Journal*, 886, 105, doi: [10.3847/1538-4357/ab4e1d](https://doi.org/10.3847/1538-4357/ab4e1d)